RSC Advances

PAPER

View Article Online
View Journal | View Issue

Cite this: *RSC Adv.*, 2017, **7**, 34609

MOF-derived hierarchical ZnO/$ZnFe_2O_4$ hollow cubes for enhanced acetone gas-sensing performance†

Xiang Ma,[ab] Xinyuan Zhou,[ab] Yan Gong,[ab] Ning Han,[a] Haidi Liu[a] and Yunfa Chen*[a]

Received 20th April 2017
Accepted 28th June 2017

DOI: 10.1039/c7ra04437b

rsc.li/rsc-advances

ZnO/$ZnFe_2O_4$ hollow cube composites with heterogeneous structure are synthesized by a facile strategy through simple and direct pyrolysis of Fe^{III}-modified Zn-based metal–organic frameworks. The as-synthesized ZnO/$ZnFe_2O_4$ hollow cubes have well-defined cube morphology with an ~2 μm and multiple porous shell constructed from interpenetrated ZnO and $ZnFe_2O_4$ heterogeneous nanoparticles, providing structurally combined mesoporous channels for facilitating the diffusion and surface reaction of gas molecules. In addition, a comparative sensing performance investigation between ZnO/$ZnFe_2O_4$ hollow cubes and singular ZnO demonstrates that, in contrast with ZnO, the ZnO/$ZnFe_2O_4$ hollow cubes show significantly enhanced chemical sensing sensitivity towards low-concentration acetone. Furthermore, the ZnO/$ZnFe_2O_4$ hollow cubes exhibit good reproducibility and selectivity towards gaseous acetone. The enhanced sensing performance of the MOF-derived ZnO/$ZnFe_2O_4$ hollow cubes is ascribed to the unique hierarchical structure with high specific surface area, abundant exposed active sites with surface-adsorbed oxygen species and heterojunctions formed at the interfaces between ZnO and $ZnFe_2O_4$.

1. Introduction

Gas sensors based on metal oxide semiconductors have received widespread interest during the past decades owing to their low power consumption, easy manufacture, low cost, as well as portable characteristics in the detection of various explosives, and harmful, and toxic gases.[1–3] To date, many metal oxide semiconductors such as ZnO,[4] SnO_2,[5] In_2O_3,[6] α-Fe_2O_3,[7] NiO,[8] and WO_3 (ref. 9) have been extensively investigated for gas sensing. It is well acknowledged that the performance of sensors including increased sensitivity, enhanced selectivity, outstanding reproducibility and long-term stability strongly depend on the gas sensing materials so that great efforts have been made to enhance the sensing properties such as noble metal loading,[10] designing novel material structures,[11] and construction of heterojunctions.[12] These efforts have indeed improved the sensing properties based on the fact that surface morphology, microstructure, crystalline size and composition could affect the sensing behaviors of the metal oxide semiconductors.[13–15] Hollow micro-/nanostructures have attracted widespread interest in gas sensors because the unique structure offer large specific surface area with abundant active sites, modulative interfacial electron transfers with enhanced redox capacities compared with their singular solid building block units.[16–18] The self-sacrificial template strategy based on thermolysis of solid precursors remains the most attractive one in the fabrication of hollow micro-/nanostructures and selecting the right template material is the key factor, as the self-sacrificial precursor should have the ability to be removed easily under thermal annealing condition as well as preserve the original stereoscopic shape.

Metal–organic frameworks (MOFs) are emerging as a class of very important materials offering high levels of porosity with considerable control over pore size and composition. Such properties play a crucial role in functional applications in gas adsorption,[19] sensing,[20] and catalysis.[21] Besides, the morphology of MOFs can be easily tuned through different metal ions and organic bridging ligands under different synthesis conditions.[22–26] Utilizing MOFs as templates offers a valid strategy for designing novel structure of porous carbon and metal oxides composites. For example, $NiCo_2O_4$/NiO hollow dodecahedra composite were synthesized by thermolysis of Ni containing ZIF-67 MOFs as template for enhanced lithium-ion battery.[27] α-Fe_2O_3 porous nanorods were prepared from MIL-88A MOFs with enhanced gas sensing properties.[28] MOF-5 was employed as template to fabricate hierarchical hollow ZnO nanocages with enhanced VOCs gas-sensing performance.[29] Fe_3C nanocrystallite embedded N-doped carbon matrix derived

[a]State Key Laboratory of Multiphase Complex System, Institute of Process Engineering, Chinese Academy of Sciences, Beijing, 100190, China. E-mail: chenyf@ipe.ac.cn; Tel: +86 1082544896

[b]University of Chinese Academy of Sciences, No. 19A Yuquan Road, Beijing, 100049, China

† Electronic supplementary information (ESI) available. See DOI: 10.1039/c7ra04437b

from MIL-88B@ZIF-8 dual-MOFs exhibit remarkable electrocatalytic activity for the ORR in a basic electrolyte.[30] These great progresses were achieved due to the remarkable properties with selectable metal ion, multifunctional organic ligands, well-developed porosity and diverse morphologies of MOFs.

Among many metal oxide semiconductors, ZnO is an attractive n-type semiconductor with a direct wide bandgap (3.37 eV) as a popular gas sensing material because of its relatively high sensitivity and ease of fabrication.[31] However, the sensing properties of pure ZnO are still unsatisfactory for applications in real industrial purposes due to the high operating temperature and poor selectivity.[32] Recently, many reported investigations have demonstrated that the sensing performances of ZnO could be improved by the heterostructure formation techniques. For example, Qu *et al.* have fabricated gas sensors using ZnO/$ZnCo_2O_4$ hollow core–shell nanocages synthesized by the thermolysis of ZIF-8/Co–Zn hydroxide precursor, showing enhanced sensitivity to xylene and excellent reversibility.[33] Liu *et al.* have synthesized $ZnFe_2O_4$ nanoparticles decorated on ZnO microflowers by a simple mild solution method, demonstrating higher response to acetone compared with single ZnO microflower.[34] Although some improvements had been accomplished, there still existed some unnegligible drawbacks related to the unsatisfactory low detection limit of the sensing materials.

In this work, we show a generally applicable strategy for the synthesis of ZnO/$ZnFe_2O_4$ hollow cubes which includes the synthesis of Fe^{III}-modified IRMOF-3 cubes nanostructure precursor and subsequent transformation to uniform ZnO/$ZnFe_2O_4$ hollow cubes by thermal annealing of the as-prepared precursor in air atmosphere. Moreover, gas sensors based on the above products were fabricated, and their gas sensing performance was investigated. It is revealed that the ZnO/$ZnFe_2O_4$ hollow cubes displayed a higher response to acetone at a lower working temperature than the singular ZnO particles. The formation of the heterojunction between ZnO and $ZnFe_2O_4$ and porous structure of ZnO/$ZnFe_2O_4$ materials are likely to be the sources of the enhancement in gas sensing properties.

2. Experimental

2.1 Materials

$Zn(NO_3)_2 \cdot 6H_2O$ was purchased from Aladdin. $Fe(acac)_3$ and 2-aminoterephthalic acid (H_2N-BDC) were purchased from Alfa. Polyvinyl pyrrolidone (PVP, M. W. 30 000), *N*,*N*-dimethylformamide (DMF) and ethanol were purchased from Sinopharm. All chemicals were used directly without further purification. The water was made from Millipore Milli-Q water (15 MΩ cm).

2.2 Preparation of ZnO/$ZnFe_2O_4$ hollow cubes

The Fe^{III}-modified IRMOF-3 precursor was synthesized according to the previously reported method.[35] Typically, 3.34 g of $Zn(NO_3)_2 \cdot 6H_2O$, 4.32 g of $Fe(acac)_3$, 0.68 g of H_2N-BDC and 14.2 g of PVP were dispersed into a 480 mL of mixed solvent (DMF/ethanol = 5 : 3). The resulting solution was stirred for 1 h to obtained a uniformly dissolution of the reactants, and then refluxed at 100 °C for 8 h. The umber precipitant was washed with ethanol several times by centrifugation. As-obtained precipitant was dried at 80 °C under vacuum for 24 h. The collected powders were used as precursors to prepare ZnO/$ZnFe_2O_4$ samples by temperature-programmed thermal decomposition process with a slow rate of 1 °C min^{-1} from room temperature to 500 °C and kept at 500 °C for 2 h under air atmosphere. The synthesis of singular ZnO nanoparticle and singular $ZnFe_2O_4$ are presented in the ESI.†

2.3 Characterization of materials

Powder X-ray diffraction (XRD) patterns of the catalysts were measured on a Panalytical X'Pert PRO system using Cu-Kα radiation. Thermogravimetric analysis (TGA) was performance on a NETZSCH STA449F3 apparatus with a heating rate of 10 °C min^{-1} from 35 °C to 900 °C under air atmosphere. The N_2 adsorption–desorption isotherms were measured on automatic surface analyzer (SSA-7300, China). Before the measurement, the samples were outgassed at 100 °C for 10 h. The morphology of materials were characterized by field-emission scanning electron microscopy (SEM) *via* an electron microscope (JEOL 2100F, operating at 15 kV) and transmission electron microscopy (TEM) with an accelerating voltage of 200 kV. The chemical compositions of the samples were measured by energy dispersive X-ray spectrometry (EDS) that was attached on TEM. Surface species of the as-prepared catalysts were determined by X-ray photoelectron spectroscopy (XPS) using an XLESCALAB 250 Xi electron spectrometer from VG Scientific with a monochromatic Al Kα radiation.

2.4 Gas sensing measurement

The gas sensing experiments were performed on a homemade tube-furnace sensor test system. The diameter of tube-furnace is 5 cm, and length is 1 m. Typically, two Pt wires were fixed on an Al_2O_3 substrate by silver paste (Wuhan Double bond Chemical Co., Ltd,. China). After that, a certain amount of the as-synthesized ZnO/$ZnFe_2O_4$ powders were dispersed into ethanol and then drop-coated onto the Al_2O_3 substrate to form a film. The obtained gas sensor was placed into the tube-furnace and kept at thermostable temperature of 300 °C over night to ensure good ohmic contacts. The ohmic contacts were confirmed by the Keithley 2601 Sourcemeter (Keither Instrument Inc., USA) with a rectangular sweep voltage (continuously set at 5 V, 2.5 V, 0 V, −2.5 V, and −5 V). The detected gases with different concentrations were obtained through mixing the synthetic air (20.9 vol% O_2, 79.1 vol% N_2) and standard gases (50 ppm in synthetic air for acetone, ethanol, toluene, benzene and 50 ppm in N_2 for formaldehyde and ammonia, Beijing Hua Yuan Gas Chemical Industry Co., Ltd., China) in a mixer before entering into the tube furnace. The total flow velocity of gases is 600 mL min^{-1}. The voltage bias was fixed at 5 V and the current was recorded using Keithley 2601 sourcemeter. The sensor response is defined as $R = R_{air}/R_{gas}$ where R_{air} and R_{gas} are the sensor resistance in air and in the test gas, respectively. The response time is defined as the time required for sensor resistance reaching to 90% of the final value after exposed to the

target gas. The recovery time is defined as the time required for reducing to 10% of the saturation value after exposed to clean air.

3. Result and discussion

3.1 Characterizations of materials

The crystallographic structure of the synthesized Fe^{III}-modified IRMOF-3 precursor and $ZnO/ZnFe_2O_4$ materials were determined by XRD measurements. The detected diffraction peaks of Fe^{III}-modified IRMOF-3 precursor in Fig. 1a are in good agreement with previously reported simulated IRMOF-3 patterns.[36] It was confirmed that the crystal structure of IRMOF-3 could be maintained in the precursor even adding the Fe ions, which may be attributed to a small quantity of Fe doping.[37] It should be pointed out that the intensities of diffraction peaks at $2\theta = 6.9^\circ$ and 9.7° in Fe^{III}-modified IRMOF-3 precursor have been changed compared with IRMOF-3 which could be induced by Fe ions modification. Fig. 1b illustrates the XRD patterns of the final products after annealing in air which are indexed to the combined wurtzite crystal phases of ZnO (JCPDS no. 036-1451) and spinel $ZnFe_2O_4$ (JCPDS no. 077-0011), indicating co-existing of two heterogeneous phases in the synthesized products including ZnO and $ZnFe_2O_4$. It should be pointed out that the diffraction peaks of $ZnFe_2O_4$ are not obvious, probably because of the large content of ZnO or the overlap of $ZnFe_2O_4$ and ZnO peaks. But obviously, the color of $ZnO/ZnFe_2O_4$ is very different from that of bare ZnO shown in Fig. 1b, from which the heterogeneous phases get confirmed. The XRD patterns of singular ZnO and $ZnFe_2O_4$ are shown in the Fig. S1 and S2,† which is indexed to the wurtzite crystal phase of ZnO and spinel $ZnFe_2O_4$ respectively. The thermogravimetric analysis (TGA) of Fe^{III}-modified IRMOF-3 precursor was investigated and shown in Fig. 1c. A two-step thermal decomposition process was observed includes the first weight loss of 8% from 35 °C to 150 °C which is attributed to the loss of adsorbed H_2O and alcohol. While the second weight loss was about 60.1% between 150 °C to 500 °C, which most likely resulted from the decomposition of organic ligands and PVP surfactant resulting in releasing CO_2, NO_x and H_2O. No obvious weight loss was observed after 500 °C and $ZnO/ZnFe_2O_4$ was subsequently formed. The N_2 adsorption–desorption isotherms of the as-prepared $ZnO/ZnFe_2O_4$ material is presented in Fig. 1d, and feature type IV isotherm, indicating mesoporous properties of $ZnO/ZnFe_2O_4$ hollow cubes. The pore diameter of $ZnO/ZnFe_2O_4$ is about 8 nm in the inset of Fig. 1d and the BET surface area is 50 $m^2\ g^{-1}$. Evidently, the as-prepared $ZnO/ZnFe_2O_4$ hollow cubes possess typical hierarchical structures with micro-/nanoscale particulate systems, which offer sufficiently interface and active sites for the gaseous adsorption–desorption and the chemical reaction between analyte molecules and $ZnO/ZnFe_2O_4$. The N_2 adsorption–desorption isotherm of the singular ZnO and $ZnFe_2O_4$ nanoparticles are shown in Fig. S3.†

The morphologies and microstructures of Fe^{III}-modified IRMOF-3 precursors and their derivative $ZnO/ZnFe_2O_4$ hollow cubes are shown in Fig. 2. The Fe^{III}-modified IRMOF-3

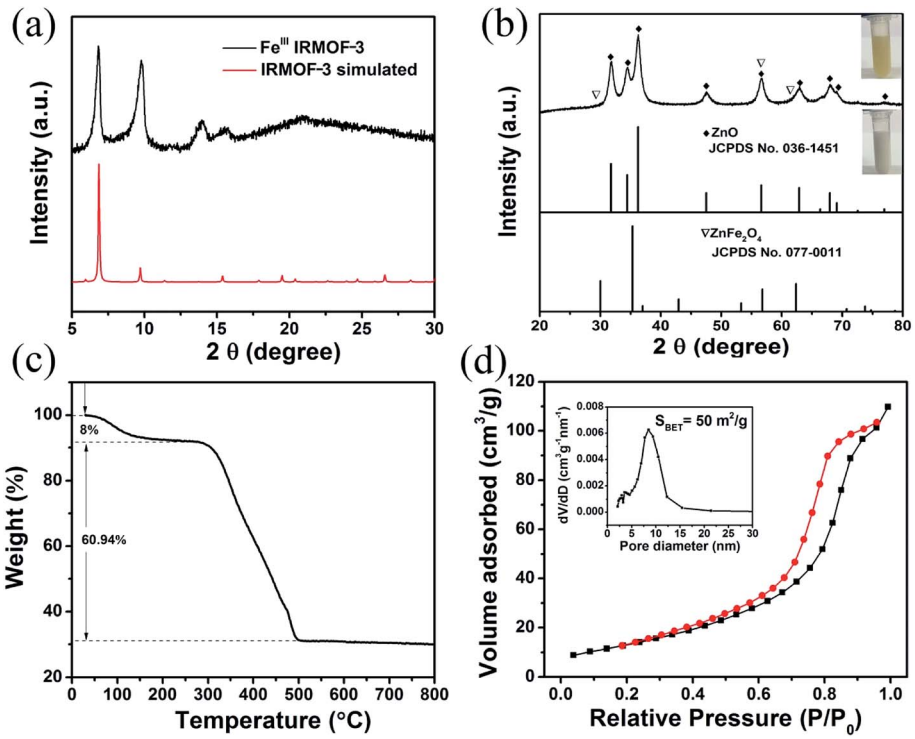

Fig. 1 XRD patterns of (a) Fe^{III}-modified IRMOF-3 precursor and (b) $ZnO/ZnFe_2O_4$ hollow cubes (the insets are the photographs of $ZnO/ZnFe_2O_4$ and singular ZnO); (c) TGA curve of Fe^{III}-modified IRMOF-3 precursor; (d) N_2 adsorption–desorption isotherm of the $ZnO/ZnFe_2O_4$ hollow cubes (the inset is the corresponding BJH pore size distribution).

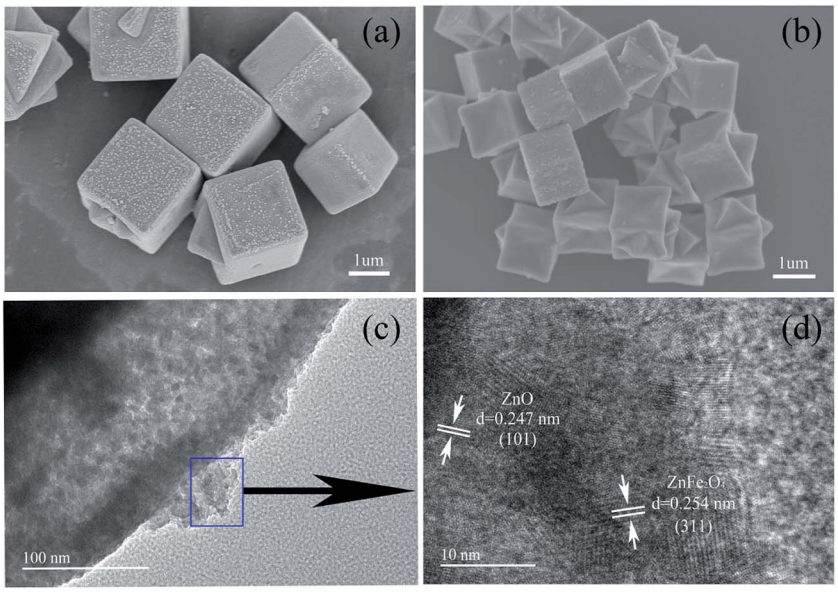

Fig. 2 SEM images of (a) Fe^{III}-modified IRMOF-3 precursor and (b) $ZnO/ZnFe_2O_4$ hollow cubes; (c) TEM image of the edge of $ZnO/ZnFe_2O_4$ hollow cubes; (d) HRTEM image taken from the frame marked region in (c).

precursors in Fig. 2a illustrated well-defined cube morphologies with average particle sizes of about 2 μm. As shown in Fig. 2b, after calcination process at 500 °C, both the cube shape and size of the precursors remain intact except that the outside surface become little collapsing inwards indicating the hollow structure of $ZnO/ZnFe_2O_4$ cubes. The hollow structure is further confirmed from the TEM image in Fig. 2c, which shows the edge of $ZnO/ZnFe_2O_4$ composites with clearly hollow shell and the shell of individual $ZnO/ZnFe_2O_4$ hollow cubes was constructed by ultrafine interconnected nanoparticles. Moreover, the EDS mapping spectra of selected individual $ZnO/ZnFe_2O_4$ hollow cube in Fig. 3 show that the elements of Zn and Fe are uniformly dispersed within the shell, which further confirms the hollow structure of $ZnO/ZnFe_2O_4$. It should be pointed out that the Fe content is relative low (3.34 wt%) in $ZnO/ZnFe_2O_4$ sample. Fig. 2d shows the HRTEM image of selected region from Fig. 2c, indicates the $ZnO–ZnFe_2O_4$ hetero-junctions of in-shell nanoparticles with two sets of clear lattice fringes and unclear interfacial domains, indicative of crystalline detects and distortions due to two-phase transition at heterogeneous

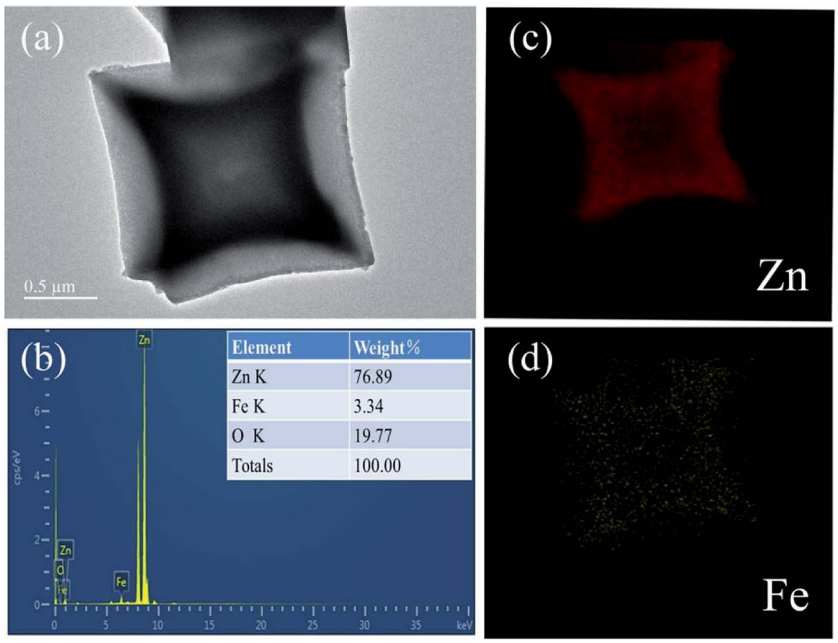

Fig. 3 (a) TEM image of $ZnO/ZnFe_2O_4$ hollow cube; (b) EDS analysis of the elemental composition of $ZnO/ZnFe_2O_4$ hollow cube; (c and d) EDS mapping images of $ZnO/ZnFe_2O_4$ hollow cube.

interfaces. The lattice spacings of 0.247 nm and 0.254 nm correspond to the (101) plane of the wurtzite ZnO structure and the (311) plane of the spinel $ZnFe_2O_4$ structure, respectively. The good interfacial contact between ZnO and $ZnFe_2O_4$ contribute to easy electron transfer between the two phases, which is favorable for the enhanced gas sensing performances. The TEM and SEM images of singular ZnO and $ZnFe_2O_4$ are shown in Fig. S4.†

XPS analysis was performed to examine the surface chemical composition and valence state of the elements of the as-synthesized ZnO/$ZnFe_2O_4$ sample, and the XPS spectra are presented in Fig. 4. Fig. 4a shows the wide spectrum of the ZnO/$ZnFe_2O_4$ sample, confirming the existence of Zn, Fe and O elements. Zn 2p spectrum in Fig. 4b displays two asymmetric peaks, corresponding to the Zn $2p_{1/2}$ and Zn $2p_{3/2}$ states of Zn 2p orbits, respectively. The fitting peaks with binding energy of 1045.1 eV and 1022.0 eV are assigned to Zn $2p_{1/2}$ and Zn $2p_{3/2}$ photoelectron responses of spinel-structural $ZnFe_2O_4$, and other two fitting peaks located at 1044.4 eV and 1021.3 eV are assigned to divalent Zn in the ZnO,[38] which is also in accordance with singular ZnO sample presented in Fig. S4.† As for Fe 2p spectrum in Fig. 4c, the binding energy at 724.7 eV and 710.4 eV are ascribed to Fe $2p_{1/2}$ and Fe $2p_{3/2}$. The shake-up satellite peaks at binding energy are at range of 715.7–720.0 eV, which are characteristic of Fe^{3+} states in spinel $ZnFe_2O_4$ phase.[39] The XPS signal of Fe 2p spectrum is weak because of the relative low content of Fe element. Besides, the asymmetrical O 1s signal can be fitted with three components: one peak at binding energy of 530.4 eV is attributed to the lattice oxygen; another peak at the medium with binding energy of 532.8 eV is assigned to the surface adsorbed oxygen and the small peak at binding energy of 533.1 eV is ascribed to the adsorbed OH groups and molecular water.[40–42] It is well known that the surface-absorbed oxygen species is closely with the electron-donor oxygen vacancies, which adsorb the oxygen molecules, and ionize them into reactive surface adsorbed oxygen species (O_2^-, O^-, O^{2-}) which is related to the gas sensing performance of sensing material. The contents of adsorbed oxygen species in ZnO/$ZnFe_2O_4$ are clearly higher than that of singular ZnO (29.4% for ZnO/$ZnFe_2O_4$ and 23.7% for ZnO). Therefore, it is anticipated that the ZnO/$ZnFe_2O_4$ sample performs a better gas-sensing behavior than the singular ZnO counterparts.

3.2 Gas sensing performance

To demonstrate the significantly enhanced gas sensing properties of the as-prepared ZnO/$ZnFe_2O_4$ hierarchical hollow cubes with interpenetrated nanoparticles as blocking units, the singular ZnO nanoparticles were chosen as blank reference. It is well-known that the operating temperature has a great impact on the reaction between the adsorbed gas and sensing materials. Therefore, the temperature dependent properties of the as-fabricated gas sensors were measured first. As shown in Fig. 5a, the response of the two kinds of sensors increased with the increasing temperature until the value reached maximum at an optimum operating temperature, and then decreased with further increasing of the operating temperature. The optimum operating temperature ranges from 200 °C to 250 °C for the synthesized ZnO/$ZnFe_2O_4$ sample, which is lower than that of 250 °C to 300 °C for the singular ZnO counterparts. Therefore, the further measurements were performed at 250 °C. Fig. 5b

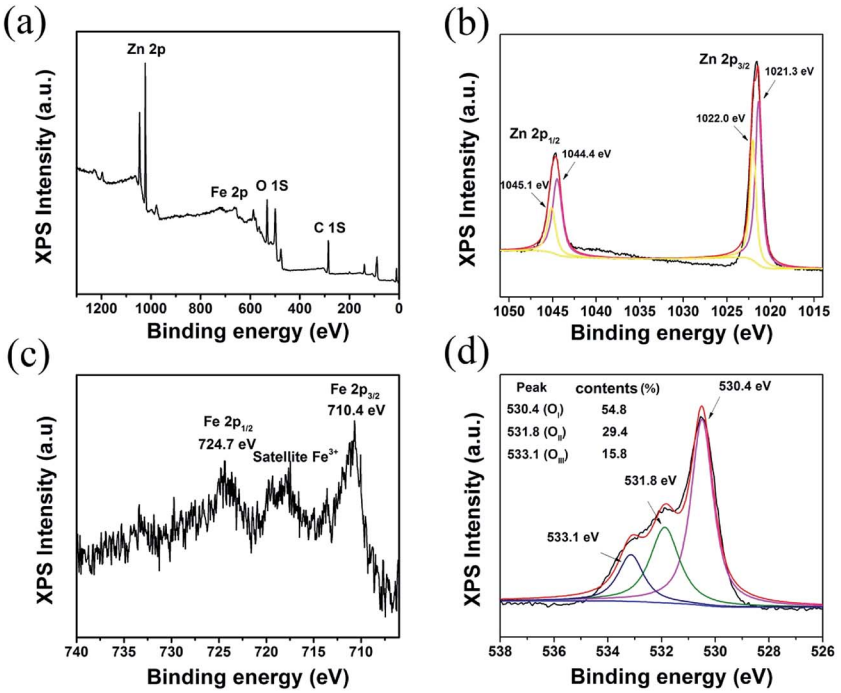

Fig. 4 XPS spectra of (a) survey of the spectra; (b) Zn 2p spectra; (c) Fe 2p spectra and (d) O 1s spectra of the as-prepared ZnO/$ZnFe_2O_4$ sample. (O_I: lattice oxygen; O_{II}: surface adsorbed oxygen; O_{III}: adsorbed OH groups and molecular water).

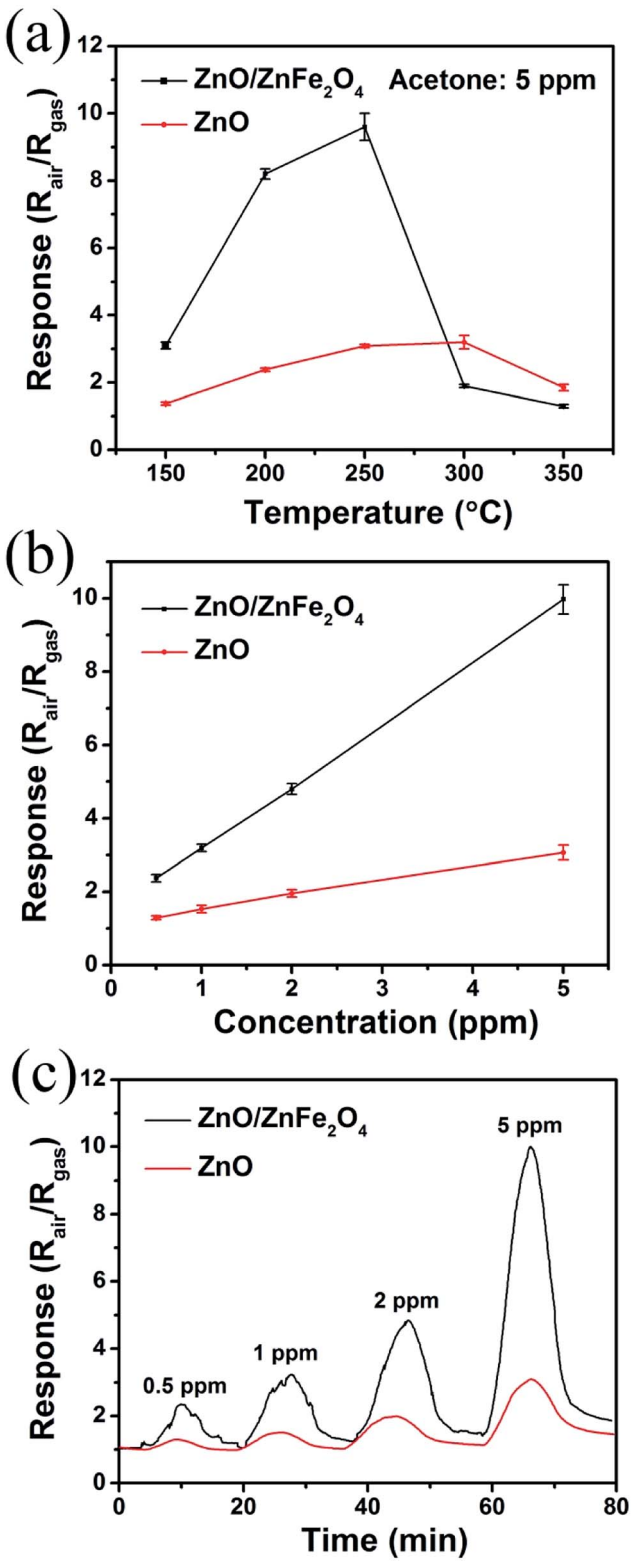

Fig. 5 (a) Gas sensing response of $ZnO/ZnFe_2O_4$ hollow cubes and singular ZnO to 5 ppm acetone at different operating temperature; (b) comparison of responses between $ZnO/ZnFe_2O_4$ hollow cubes and singular ZnO operating at 250 °C; (c) the dynamic response–recovery curve of $ZnO/ZnFe_2O_4$ hollow cubes and singular ZnO towards different acetone concentration.

provides the gas responses of the two kinds of gas sensors as a function of the concentration of acetone at 250 °C. The results showed that the gas responses of the two kinds of sensors increased with the increasing concentration of acetone and almost linear response *versus* concentration trend for the ZnO/$ZnFe_2O_4$ hollow cubes indicates a perfect potential in the quantitative gas analysis. It is obvious that the $ZnO/ZnFe_2O_4$ hollow cubes revealed a quite enhanced gas response compared with that of singular ZnO at each concentration of acetone. It can be observed that when the acetone concentration was as low as 0.5 ppm, it still had a response of 2.4, indicating the ultra-low detection limit of $ZnO/ZnFe_2O_4$ hollow cubes. Moreover, the response of $ZnO/ZnFe_2O_4$ hollow cubes towards 5 ppm acetone is much higher than that of singular $ZnFe_2O_4$ nanoparticles which is only 1.36 at 250 °C. The dynamic response–recovery curve of $ZnO/ZnFe_2O_4$ hollow cubes and singular ZnO towards different acetone concentrations at 250 °C are shown in Fig. 5c. The response/recover times are 5.9/7.4 min, 5.7/6.5 min, 5.8/6.3 min, 5.6/6.0 min for 0.5, 1.0, 2.0, 5.0 ppm acetone, respectively, longer than other $ZnO/ZnFe_2O_4$-based sensors towards relative high-concentration acetone. This may be ascribed to the slow surface adsorption–desorption kinetics of gaseous acetone molecules for the lower concentration acetone detection in our selected experimental conditions.[43,44] Importantly, the ZnO/$ZnFe_2O_4$ hollow cubes sensor performs higher response towards acetone sensing compared with previously reported ZnO/$ZnFe_2O_4$ sensing materials with different microstructure and summarized in Table 1.

Other important gas sensing parameters including reproducibility long-term stability and selectivity were also investigated using $ZnO/ZnFe_2O_4$ hollow cubes as sensing material and shown in Fig. 6. Obviously, the $ZnO/ZnFe_2O_4$ hollow cubes illustrate good reproducibility towards 5 ppm acetone at 250 °C operating temperature after six on–off cycles, and the response value is $9.4 \pm 7.1\%$. Moreover, $ZnO/ZnFe_2O_4$ hollow cubes based sensor to 5 ppm acetone at a constant working temperature of 250 °C during a long-term stability measurement of 14 days was conducted. The results showed that the response of the ZnO/$ZnFe_2O_4$ sensor changed a little, which confirmed good stability of $ZnO/ZnFe_2O_4$ hollow cubes. In addition, the selectivity of $ZnO/ZnFe_2O_4$ hollow cubes was also tested at 250 °C towards 5 ppm teat gases including acetone, ethanol, formaldehyde, toluene, benzene and ammonia which are common indoor gaseous contaminants. Significantly, the $ZnO/ZnFe_2O_4$ sensor possesses good selectivity to detect acetone at 250 °C, and shows low response or almost insensitive to other interference gases at the same operating temperature and shown in Fig. 6c. The good selectivity for acetone may be ascribed to the bond dissociation energy (BDE) of different gases. The BDE of H–CH_2COCH_3 (393 kJ mol^{-1}) in acetone is less than that of H–OCH_2CH_3 (436 kJ mol^{-1}) in ethanol, H–C_6H_5 (431 kJ mol^{-1}) in benzene, but similar with CH_3–C_6H_5 (389 kJ mol^{-1}) in toluene. Another factor may be associated with the number of electrons released during the redox reaction at 250 °C operating temperature presented in the following equations. Therefore, the $ZnO/ZnFe_2O_4$ hollow cubes show good selectivity towards acetone with relatively lower bond dissociation energy and more released electrons.

Table 1 Comparison of acetone sensing performance of gas sensors based on various ZnO/$ZnFe_2O_4$ microstructures

Materials	Temperature (°C)	Concentration (ppm)	Response (R_{air}/R_{gas})	Reference
$ZnFe_2O_4$/ZnO hollow microspheres	320	100	7.5	45
$ZnFe_2O_4$/ZnO microflowers	250	50	8.3	34
$ZnFe_2O_4$ decorated ZnO rod	260	50	3.4	46
$ZnFe_2O_4$ nanosheets on ZnO sphere	250	10	4.8	47
ZnO/$ZnFe_2O_4$ hollow cubes	250	5	9.4	This work

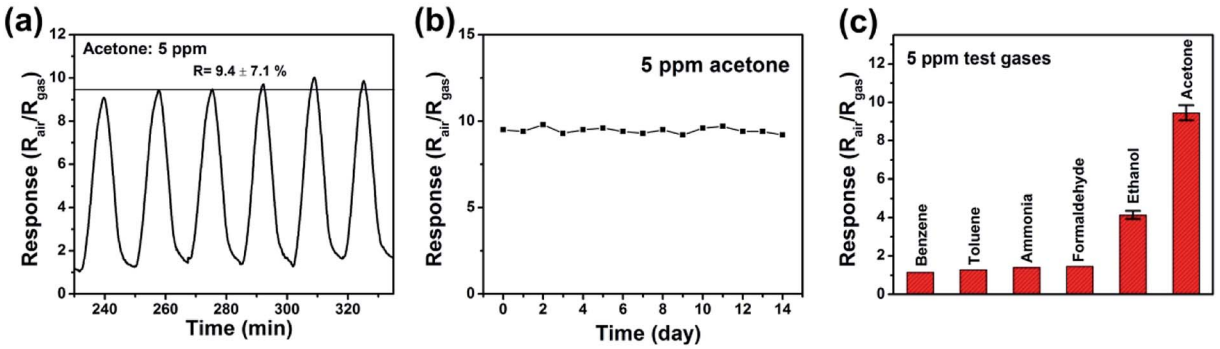

Fig. 6 (a) The reproducibility of ZnO/$ZnFe_2O_4$ hollow cubes towards 5 ppm acetone at 250 °C operating temperature; (b) the long-term stability test of ZnO/$ZnFe_2O_4$ hollow cubes towards 5 ppm acetone at 250 °C; (c) the selectivity test of ZnO/$ZnFe_2O_4$ hollow cubes for 5 ppm teat gaseous acetone, ethanol, formaldehyde, toluene, benzene and ammonia at 250 °C operating temperature.

The above results demonstrate that ZnO/$ZnFe_2O_4$ hollow cubes with enhanced sensing performance having the potential for the detection of low-concentration acetone.

$$CH_3COCH_3 + 8O_{(ads)}^- \rightarrow 3CO_2 + 3H_2O + 8e^- \quad (1)$$

$$C_6H_6 + 15O_{(ads)}^- \rightarrow 6CO_2 + 3H_2O + 15e^- \quad (2)$$

3.3 Gas sensing mechanism

The enhanced gas sensing performance of ZnO/$ZnFe_2O_4$ hollow cubes can mainly be attributed to the mesoporous nanostructure and formation of ZnO–$ZnFe_2O_4$ heterojunctions at the ZnO/$ZnFe_2O_4$ interfaces. First of all, the hollow cube structure with mesopores can provide a high accessible surface area, thus more surface active sites are available for the sensing reactions between teat gas molecules and adsorbed oxygen ion species, contributing to higher gas sensing performance. Besides, the sensing mechanism of n-type semiconducting metal oxides can be explained in terms of depletion layers by oxygen adsorption, which may result in change in resistance of the sensor when exposed to different gas.[48,49] Fig. 7 illustrates the sensing reaction mechanism of the ZnO/$ZnFe_2O_4$ hollow cubes sensor in detecting acetone gas. When the ZnO/$ZnFe_2O_4$ expose to air, oxygen molecules can adsorb on the surface of

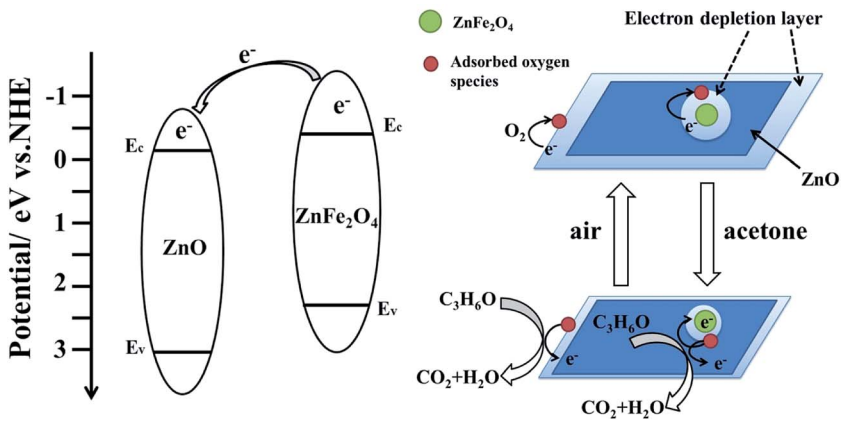

Fig. 7 Schematic diagram of the sensing reaction mechanism of the ZnO/$ZnFe_2O_4$ composites sensor for detecting acetone.

sensing materials to form surface adsorbed oxygen (O_2^-, O^-, O^{2-}) by capturing electrons from the conduction band of sensing material, leading to formation of electron deletion layer in the surface regions of both ZnO and $ZnFe_2O_4$. On the other hand, the ZnO–$ZnFe_2O_4$ hetero-junctions are created in the interface regions between ZnO and $ZnFe_2O_4$, resulting in the interfacial charge separation and the increase of free electron density and plays an important role in enhancing the gas sensing properties. Since the electron depletion layer can be generated on the surface region of ZnO, $ZnFe_2O_4$ and in the vicinity of ZnO/$ZnFe_2O_4$ interfaces, a thicker electron depletion layer and a larger amount of adsorbed negatively charged oxygen ion species are formed in ZnO/$ZnFe_2O_4$ material than the singular ZnO upon exposure to air. When the sensing material is exposed to acetone, these acetone gas molecules can react with the surface adsorbed oxygen ion species to produce CO_2 and H_2O, and release the trapped electrons back to the conduction band, which narrows the electron depletion layer and decreases the resistance of ZnO/$ZnFe_2O_4$ nanostructure sensor. Because more trapped electrons can turn back to the conduction band of the ZnO/$ZnFe_2O_4$ nanostructure than the singular ZnO, the greater resistance change can be found, thus resulting in an enhanced response.

4. Conclusions

In summary, uniform ZnO/$ZnFe_2O_4$ hollow cubes composites were synthesized by a facile strategy through simple and direct pyrolysis of Fe^{III}-modified Zn-based metal–organic frameworks. The material composition and microstructure were examined by SEM, TEM, XRD, and XPS analysis. In particular, a comparative gas sensing investigation clearly showed that the ZnO/$ZnFe_2O_4$ material exhibited better acetone-sensing performance compared with singular ZnO nanoparticles, including higher response and good reproducibility. Besides the ZnO/$ZnFe_2O_4$ material have good selectivity to acetone, indicating its promising application as gas sensor for detecting polluting gases and selectivity to acetone. The enhanced sensing properties could be mainly attributed to the unique hierarchical structure with high specific surface area, abundant exposed active sites with surface-adsorbed oxygen species and heterojunctions formed at the interfaces between ZnO and $ZnFe_2O_4$.

Acknowledgements

The authors are grateful to the Strategic Project of Science and Technology of Chinese Academy of Science (No. XDB05050400) and the National Science and Technology support (No. 2014BAC21B00).

References

1 J. H. Lee, *Sens. Actuators, B*, 2009, **140**, 319–336.
2 D. R. Miller, S. A. Akbar and P. A. Morris, *Sens. Actuators, B*, 2014, **204**, 250–272.
3 J. Zhang, X. H. Liu, G. Neri and N. Pinna, *Adv. Mater.*, 2016, **28**, 795–831.
4 Z. H. Jing and J. H. Zhan, *Adv. Mater.*, 2008, **20**, 4547–4551.
5 B. Wang, L. F. Zhu, Y. H. Yang, N. S. Xu and G. W. Yang, *J. Phys. Chem. C*, 2008, **112**, 6643–6647.
6 J. T. Zai, J. Zhu, R. R. Qi and X. F. Qian, *J. Mater. Chem. A.*, 2013, **1**, 735.
7 C. Z. Wu, P. Yin, X. Zhu, C. Z. Ouyang and Y. Xie, *J. Phys. Chem. B*, 2006, **110**, 17806–17812.
8 C. J. Dong, X. H. Xiao, G. Chen, H. T. Guan, Y. D. Wang and L. Djerdj, *RSC Adv.*, 2015, **5**, 4880–4885.
9 R. A. Kadir, W. Zhang, Y. C. Wang, J. Z. Qu, W. Wlodarski, A. P. O'Mullane, G. Bryant, M. Taylor and K. Kalantar-zadeh, *J. Mater. Chem. A.*, 2015, **3**, 7994–8001.
10 K. P. Kamioth, *Chem. Rev.*, 2008, **108**, 387–399.
11 W. T. Koo, S. J. Choi, S. J. Kim, J. S. Jang, H. L. Tuller and I. D. Kim, *J. Am. Chem. Soc.*, 2016, **138**, 13431–13437.
12 H. L. Tian, H. Q. Fan, G. Z. Dong, L. T. Ma and J. W. Ma, *RSC Adv.*, 2016, **6**, 109091–109098.
13 P. Rai, S. M. Majhi, Y. T. Yu and J. H. Lee, *RSC Adv.*, 2015, **5**, 76229–76248.
14 D. P. Volanti, A. A. Felix, M. O. Orlandi, G. Whitfield, D. J. Yang, E. Longo, H. L. Tuller and J. A. Varela, *Adv. Funct. Mater.*, 2013, **23**, 1759–1766.
15 M. S. Yao, W. X. Tang, G. E. Wang, B. Nath and G. Xu, *Adv. Mater.*, 2016, **28**, 5229–5234.
16 X. Zhou, W. Feng, C. Wang, X. D. Hu, X. W. Li, P. Sun, K. Shimance, N. Yamazoe and G. Y. Lu, *J. Mater. Chem. A.*, 2014, **2**, 17683–17690.
17 J. R. Huang, C. C. Shi, G. J. Fu, P. P. Sun, X. Y. Wang and C. P. Gu, *Mater. Chem. Phys.*, 2014, **144**, 343–348.
18 Z. C. Wu, K. Yu, S. D. Zhang and Y. Xie, *J. Phys. Chem. C*, 2008, **112**, 11307–11313.
19 X. Ma, H. D. Liu, W. M. Li, S. P. Peng and Y. F. Chen, *RSC Adv.*, 2016, **6**, 96997–97003.
20 M. Drobek, J. H. Kim, M. Bechelany, C. Valicari, A. Julbe and S. S. Kim, *ACS Appl. Mater. Interfaces*, 2016, **8**, 8323–8328.
21 J. Song, Z. Luo, D. K. Britt, H. Furukawa, O. M. Yaghi, K. I. Hardcastle and C. I. Hill, *J. Am. Chem. Soc.*, 2011, **113**, 16839–16846.
22 S. L. Zhao, H. J. Yin, L. Du, L. C. He, K. Zhao, L. Chang, G. P. Ying, H. J. Zhao, S. Q. Liu and Z. Y. Tang, *ACS Nano*, 2014, **8**, 12660–12668.
23 D. Li, H. Wang, X. Zhang, H. Sun, X. P. Dai, Y. Yang, L. Ran, X. S. Li, X. Y. Ma and D. W. Gao, *Cryst. Growth Des.*, 2014, **14**, 5856–5864.
24 S. Y. Zhang, H. Liu, C. C. Sun, P. F. Liu, L. C. Li, Z. H. Yang, X. Feng, F. W. Huo and X. H. Lu, *J. Mater. Chem. A.*, 2015, **3**, 5294–5298.
25 L. Pan, T. Mummad, L. Ma, Z. F. Huang, S. B. Wang, L. Wang, J. J. Zou and X. W. Zhang, *Appl. Catal., B*, 2016, **189**, 181–191.
26 Y. Bai, Y. B. Dou, L. H. Xie, W. Rutledge, J. R. Li and H. C. Zhou, *Chem. Soc. Rev.*, 2016, **45**, 2327–2367.
27 C. C. Sun, J. Yang, X. H. Rui, W. N. Zhang, Q. Y. Yan, P. Chen, F. W. Huo, W. Huang and X. C. Dong, *J. Mater. Chem. A.*, 2015, **3**, 8483–8848.
28 P. Y. Gao, R. Liu, H. H. Huang, X. Jia and H. B. Pan, *RSC Adv.*, 2016, **6**, 94699–94705.

29 W. H. Li, X. F. Wu, N. Han, J. Y. Chen, X. H. Qian, Y. Z. Deng, W. X. Tang and Y. F. Chen, *Sens. Actuators, B*, 2016, **225**, 158–166.
30 Y. Guan, L. Yu and X. W. Lou, *Energy Environ. Sci.*, 2016, **9**, 3092–3096.
31 P. Mitra, A. P. Chatterjee and H. S. Maiti, *Mater. Lett.*, 1998, **35**, 33–38.
32 N. S. Ramgir, M. Kaur, P. K. Sharma, N. Datta, S. Kailasaganapathi, S. Bhattacharya, A. K. Debnath, D. K. Aswal and S. K. Gupta, *Sens. Actuators, B*, 2013, **187**, 313–318.
33 F. D. Qu, H. F. Jiang and M. H. Yang, *Nanoscale*, 2016, **8**, 16349–16356.
34 C. Liu, B. Q. Wang, T. S. Wang, J. Y. Liu, P. Sun, X. H. Chuai and G. Y. Lu, *Sens. Actuators, B*, 2017, **248**, 902–909.
35 Y. J. Wu, S. L. Zhao, K. Zhao, T. X. Tu, J. H. Zheng, J. Chen, H. F. Zhou, D. J. Chen and S. X. Li, *J. Power Sources*, 2016, **311**, 137–143.
36 M. Eddaoudi, J. Kim, N. Rosi, D. Vodak, J. Wachter, M. O'Keeffe and O. M. Yaghi, *Science*, 2002, **295**, 469–472.
37 H. Sun, H. X. Su, X. Y. Ma, P. F. Zhang, X. Zhang, X. P. Dai, J. S. Gao, C. Chen and S. G. Sun, *Electrochim. Acta*, 2016, **205**, 53–61.
38 L. R. Hou, L. Lian, L. H. Zhang, G. Pang, C. Z. Yuan and X. G. Zhang, *Adv. Funct. Mater.*, 2015, **25**, 238–246.
39 Y. Hou, X. Y. Li, Q. D. Zhao and G. H. Chen, *Appl. Catal., B*, 2013, **142**, 80–88.
40 K. Jirátová, J. Mikulová, J. Klempa, T. Grygar, Z. Bastl and F. Kovanda, *Appl. Catal., A*, 2009, **361**, 106–116.
41 B. Puértolas, A. Smith, I. Vázquez, A. Dejoz, A. Moragues, T. Garcia and B. Solsona, *Chem. Eng.*, 2013, **229**, 547–558.
42 W. X. Tang, H. D. Liu, X. F. Wu and Y. F. Chen, *Ozone: Sci. Eng.*, 2014, **36**, 502–512.
43 X. W. Li, X. Zhou, H. Guo, C. Wang, J. Y. Liu, P. Sun, F. M. Liu and G. Y. Lu, *ACS Appl. Mater. Interfaces*, 2014, **6**, 18661–18667.
44 Y. Lin, W. Wei, Y. Wang, J. R. Zhou, D. M. Sun, X. D. Zhang and S. P. Ruan, *J. Alloys Compd.*, 2015, **650**, 37–44.
45 S. R. Wang, X. L. Gao, J. D. Yang, Z. Y. Zhu, H. X. Zhang and Y. S. Wang, *RSC Adv.*, 2014, **4**, 57967–57974.
46 S. R. Wang, J. X. Zhang, J. D. Yang, X. L. Gao, H. X. Zhang, Y. S. Wang and Z. Y. Zhu, *RSC Adv.*, 2015, **5**, 10048–10057.
47 X. W. Li, C. Wang, H. Guo, P. Sun, F. M. Liu, X. H. Liang and G. Y. Lu, *ACS Appl. Mater. Interfaces*, 2015, **7**, 17811–17818.
48 L. W. Wang, S. R. Wang, M. J. Xu, X. J. Hu, H. X. Zhang, Y. S. Wang and W. P. Huang, *Phys. Chem. Chem. Phys.*, 2013, **15**, 17179–17186.
49 C. X. Wang, L. W. Yin, L. Y. Zhang, D. Xiang and R. Gao, *Sensors*, 2010, **10**, 2088–2106.